Supporting information

Cu@ZIF-8 derived inverse ZnO/Cu catalyst with sub-5nm ZnO for efficient CO_2 hydrogenation to methanol

Bing Hu[a], Yazhi Yin[a], Zixin Zhong[a], Dengdeng Wu[a], Guoliang Liu[a,b]* and Xinlin Hong [a,b]*

[a]*College of Chemistry and Molecular Sciences, Wuhan University, Wuhan 430072, P. R. China.*

[b]*Wuhan-Oxford Joint Catalysis Laboratory, Wuhan 430072, P. R. China*

*** Corresponding authors:**

Email address: liugl@whu.edu.cn; hongxl@whu.edu.cn;

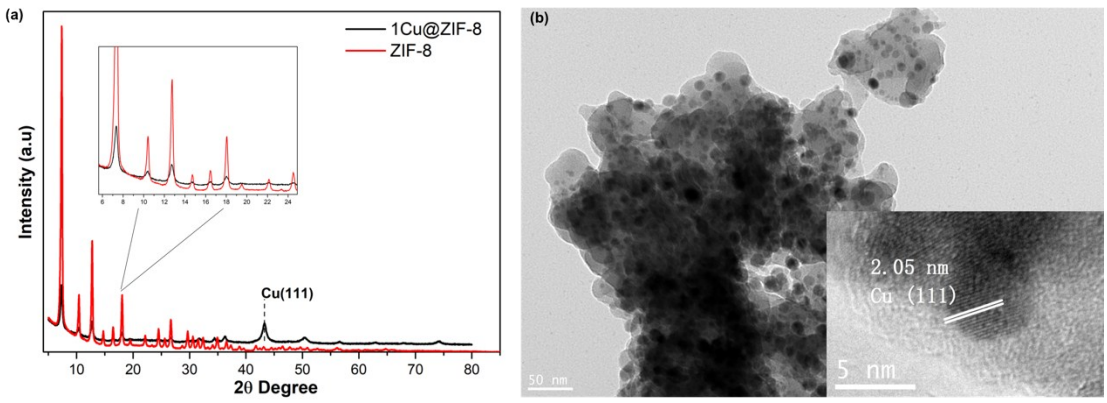

Fig. S1. (a) XRD spectra of ZIF-8 and Cu1@ZIF-8. (b) TEM image of Cu1@ZIF-8 showing the embedment of Cu nanoparticles as confirmed by the lattice fringe in the down inset.

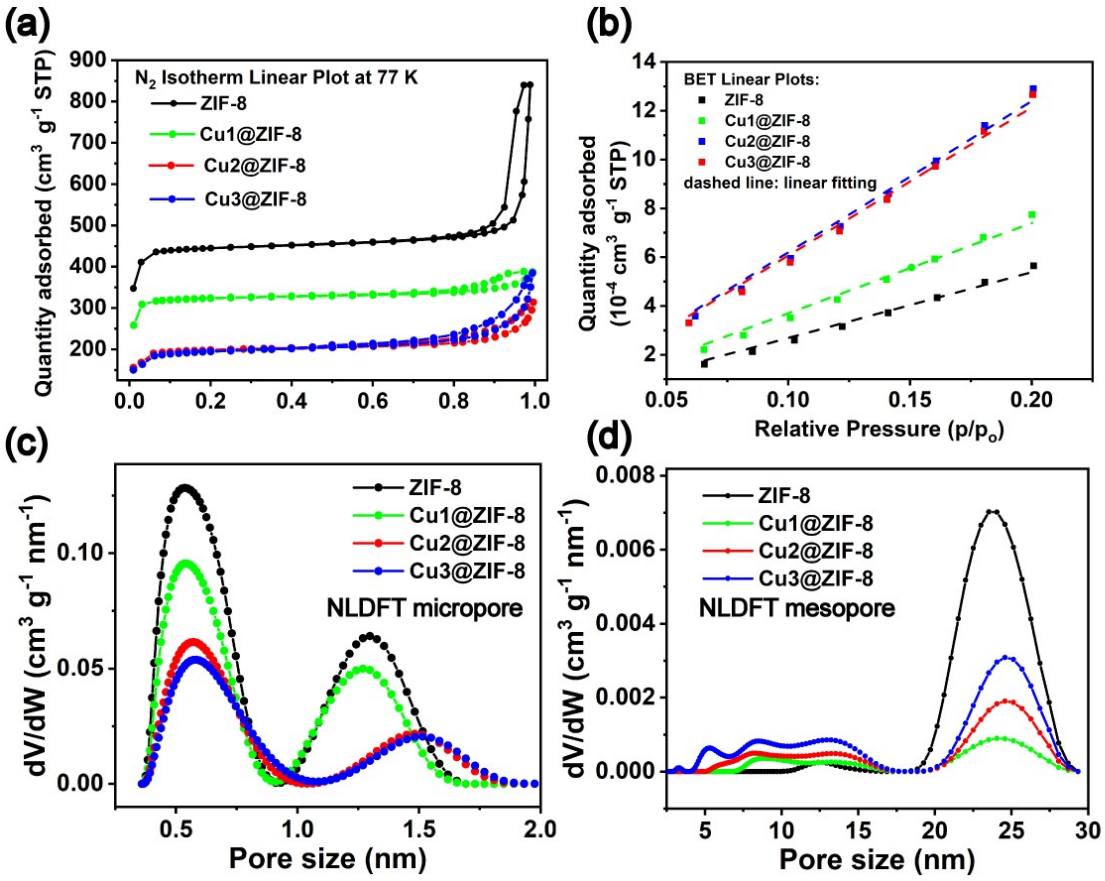

Fig. S2. N_2 physisorption (at 77 K) data of pure ZIF-8, Cu1@ZIF-8, Cu2@ZIF-8 and Cu3@ZIF-8. (a) Isothermal linear plots. (b) BET linear transform plots. (c) The micropore size distribution calculated by applying NLDFT method on the linear plots data. (d) The mesopore size distribution calculated by applying NLDFT method on the linear plots data.

Discussion on the pore structure of Cu@ZIF-8 samples.

Figs. S2(c-d) present smooth pore size distribution by applying NLDFT fitting. The model "Carbon-N_2, 2D-NLDFT Heterogeneous Surface" is used in the NLDFT fitting of the pore size distribution in ZIF-8 and Cu@ZIF-8 samples. The level of regularization is chosen so that a balance is reached between the fitting residual and roughness of the pore-size-distribution curve.

Let's first consider the total micropore volume (integration of curves in Fig.S2c), which are 0.633 cm^3 g^{-1}, 0.470 cm^3 g^{-1}, 0.282 cm^3 g^{-1}, and 0.270 cm^3 g^{-1} for ZIF-8, Cu1@ZIF-8, Cu2@ZIF-8, and Cu3@ZIF-8, respectively. We can normalize the micropore volume by taking the 0.633 cm^3 g^{-1} for ZIF-8 as 1.00. Then, those for Cu1@ZIF-8, Cu2@ZIF-8, and Cu3@ZIF-8 are 0.742, 0.446, and 0.426. Cu nanoparticles cannot generate micropores, which means the only contribution to micropore is the ZIF-8 counterpart in Cu@ZIF-8 samples. Assuming no loss of ZIF-8 and completely reduction of Cu^{2+} to Cu during the synthesis of Cu@ZIF-8, from the recipe it can be derived that the ZIF-8 weight percentages are 0.739, 0.586, and 0.485. From the normalized pore volume and the ZIF-8 weight percentage data, it can be seen that: for Cu1@ZIF-8, the micropore of ZIF-8 almost remains intact. Interestingly, the micropore size distribution curves peak at nearly identical positions for ZIF-8 and Cu1@ZIF-8 as demonstrated by the black and green line in Fig.S2c, providing evidence for ZIF-8 not infiltrated by Cu in Cu1@ZIF-8. As for Cu2@ZIF-8, this sample contains 58.6 wt% of ZIF-8 but has only 44.6% of the micropore volume of ZIF-8, this gives strong evidence for the infiltration of Cu nanoparticles into the micropores of ZIF-8. Cu3@ZIF-8 also has a slightly lower micropore volume than the expected value according to its ZIF-8 weight fraction, pointing to the inclusion of Cu within the micropore framework of ZIF-8. The micropore size distribution for Cu2@ZIF-8 and Cu3@ZIF-8 shows that the micropore volume decreases and it is apparent the pore of ZIF-8 enlarged by from 1.30 nm to 1.50 nm, which contradicts to the picture of very small Cu nanoparticles entering the ZIF-8 micropores and may point to strong interaction between Cu nanoparticles and ZIF-8.

The mesopore size distribution shown in Fig.S2d shows that ZIF-8 has the highest volume of around 25 nm mesopore than after Cu in introduced. This is because initially the mesopore is formed by stacking of ZIF-8 nanoparticles and later Cu nanoparticles take up the space

between ZIF-8 nanoparticles. For Cu1@ZIF-8, as mentioned earlier, its Cu does not affect the micropores and thus would reside on the peripheries of ZIF-8 nanoparticles, causing the largest decline in mesopore volume for ~25 nm pores. Between 2.5~17.5 nm, the pore volume of Cu@ZIF-8 samples are much larger than ZIF-8 (barely no pore distribution within this range), which should be formed by the space between adjacent Cu nanoparticles.

From the above analysis, we conclude that Cu enters the micropore framework of ZIF-8 when added Cu exceeds the loading of Cu1@ZIF-8 and the partly infiltrated Cu nanoparticles seem to expand the pore structure of ZIF-8.

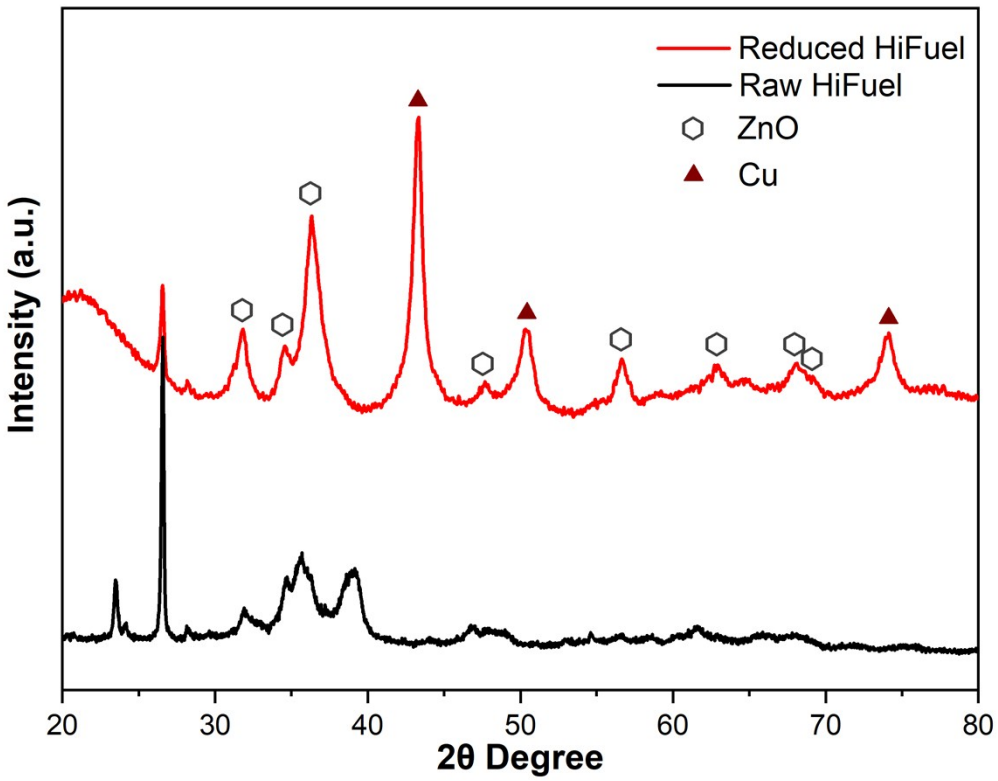

Fig. S3. XRD spectra of HiFuel before and after H_2 reduction.

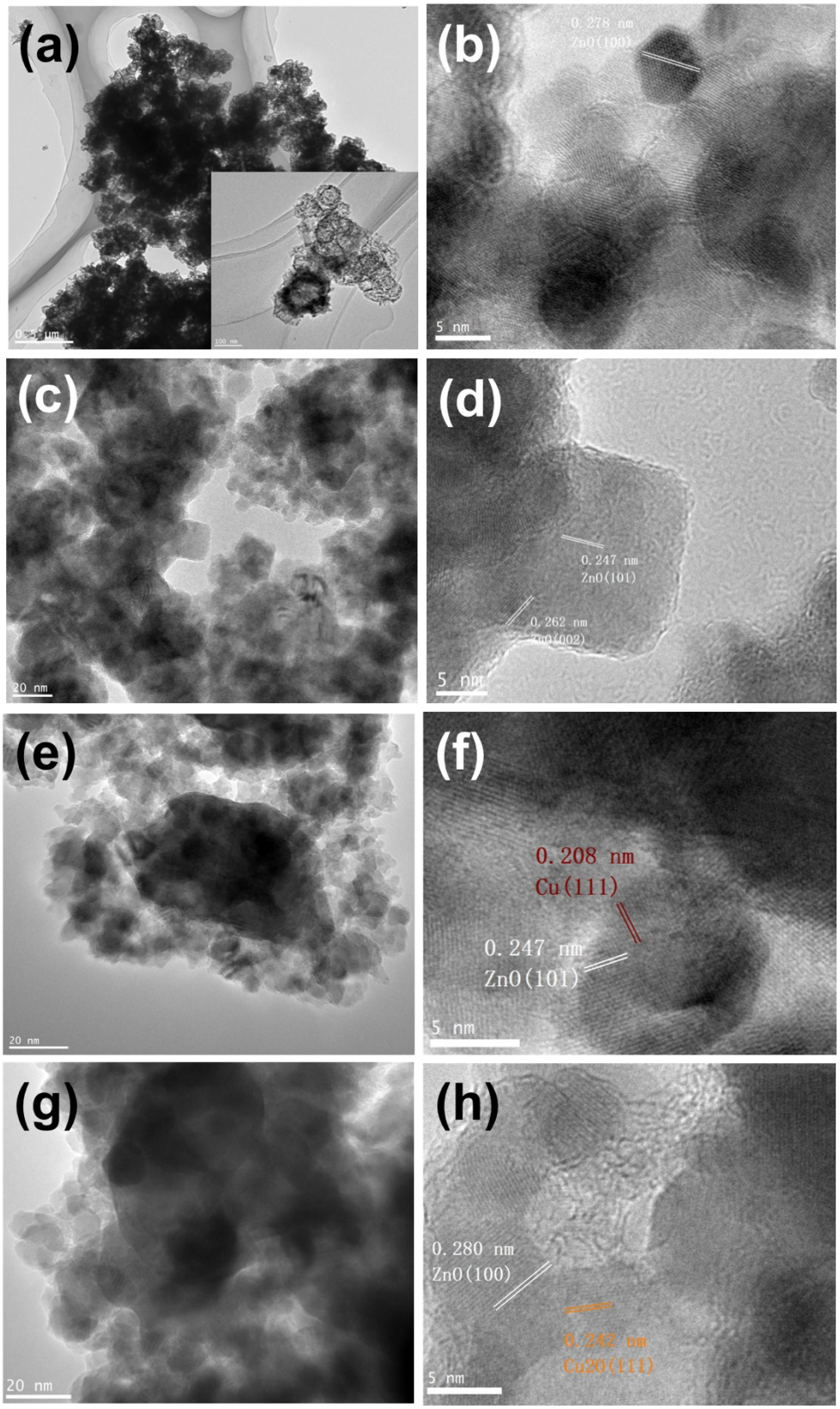

Fig. S4. TEM and HRTEM images. Before H_2 reduction: C1Z-673 (a-b) and C3Z-623 (c-d). After H_2 reduction: C2Z-673 (e-f) and C2Z-773 (g-h).

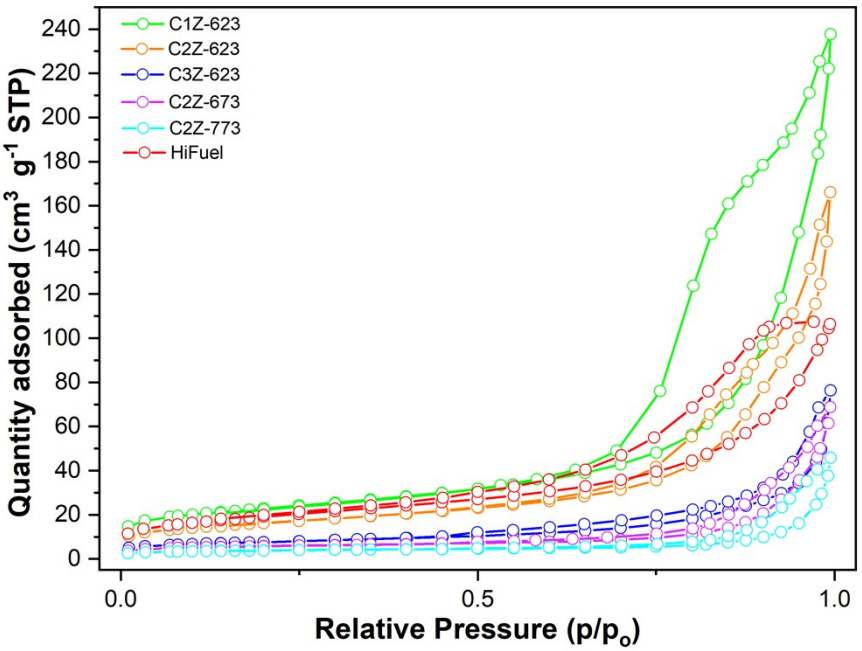

Fig. S5. N_2 physisorption isotherms of C1Z-623, C2Z-623, C3Z-623, C2Z-673, C2Z-773 and HiFuel.

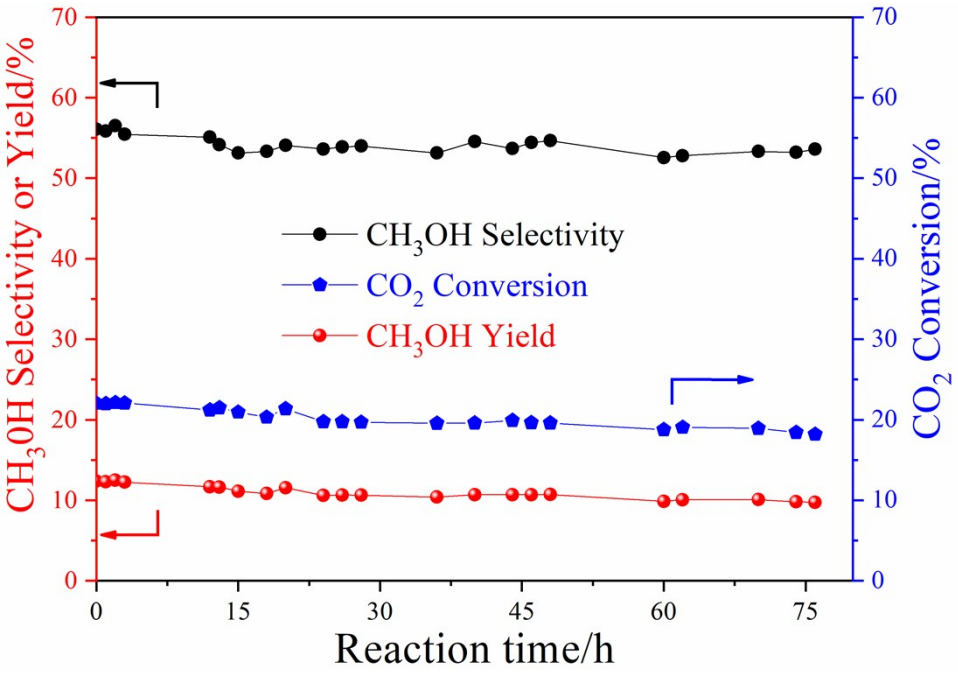

Fig. S6. Time-on-stream (TOS) test of the C2Z-623 catalyst under 533 K, 4.5 MPa, 36 mL min^{-1} H_2/CO_2 (3:1) for a total time of 76 h.

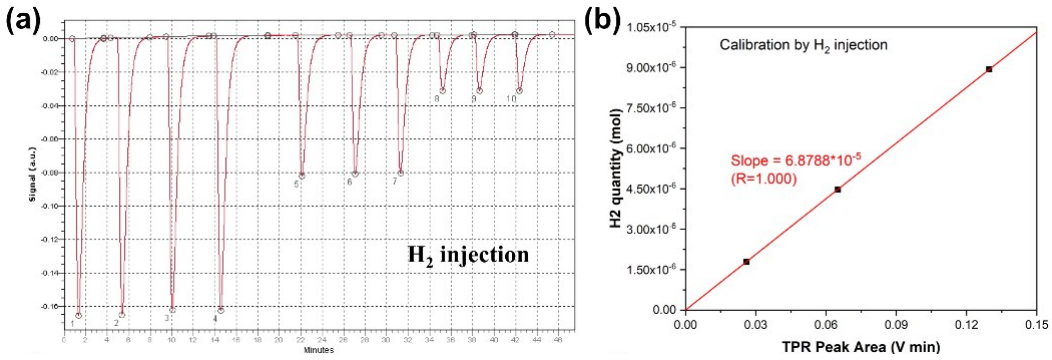

Fig. S7. Calibration of H_2 in TPD experiments by manual gas injection.

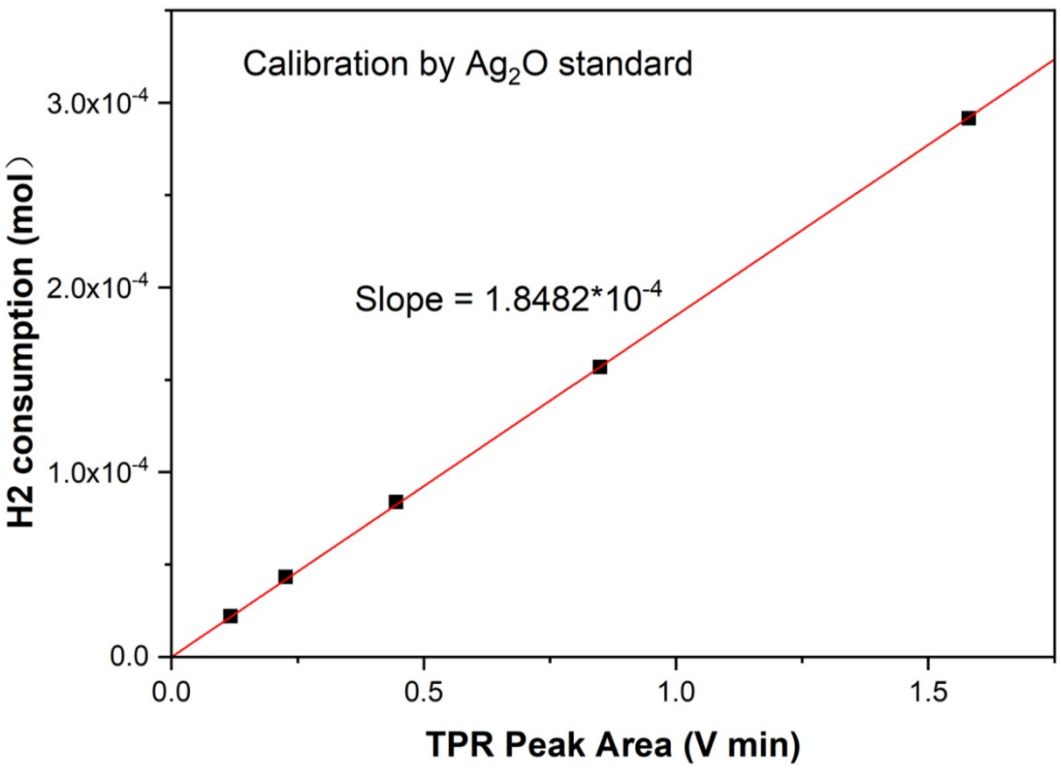

Fig. S8. Calibration of H_2 consumption by using a Ag_2O standard provided by Micromeritics.

Supplementary Paragraph

Discussion on the importance of ZIF-8 structure

For comparison, the CZ-im-673 catalyst as a reference was prepared by using impregnation method. Briefly, 0.5g ZIF-8 was dispersed into 20 mL methanol in a crucible under stirring and ultrasonication. Then 0.6719 g of copper nitrate was added and dispersed in the crucible. After that, the crucible was fitted into a heating mantle to be heated to 353 K and kept at that temperature until the solvent completely evaporates. Finally, the crucible was transferred into a muffle furnace to calcine the precursor into CuO/ZnO catalysts. The heating rate was 2 K min^{-1} and calcination went on for 2 h at 673 K. The catalyst is denoted as CZ-im-673.

The BET surface area and pore volume are 8.0 m^2 g^{-1} and 0.034 cm^3 g^{-1} (Fig. S9). The highest methanol STY is only 323 $g_{methanol}$ $kg_{catalyst}^{-1}$ h^{-1} (Fig. S10). XRD spectra (Fig. S11) of the reduced catalyst showed that the crystalline size of Cu and ZnO is 24.7 nm and 20.5 nm, respectively. We also characterized the Cu/ZIF-8 precursor formed after impregnation by XRD and TG (Fig. S12), which shows that the reticular structure of ZIF-8 collapses and $Cu_2(OH)_3NO_3$ is present in the sample. We also tried the impregnation by using $Cu(CH_3COO)_2$ as the Cu source and the solvent was removed by freeze drying, but the results were quite similar. The ZIF-8 framework collapsed and the catalytic activity was very poor. These results suggest that the ZIF-8 framework can be maintained during the prereduction of Cu^{2+} to Cu by $NaBH_4$ in our case, which is critical for the formation of the porous texture and small-sized ZnO nanoparticles. We speculate that Cu nanoparticles provide the nondeformable solid surface for the landing of in situ generated ZnO species during the calcination of Cu@ZIF-8, resulting in a strong interaction between Cu and Zn. When ionic Cu^{2+} and Zn^{2+} are both present in the precursor, the calcination leads to the separate phase evolution of CuO and ZnO, and thus big particles are formed. The structure of obtained CuO-ZnO is highly dependent on the precursors used.

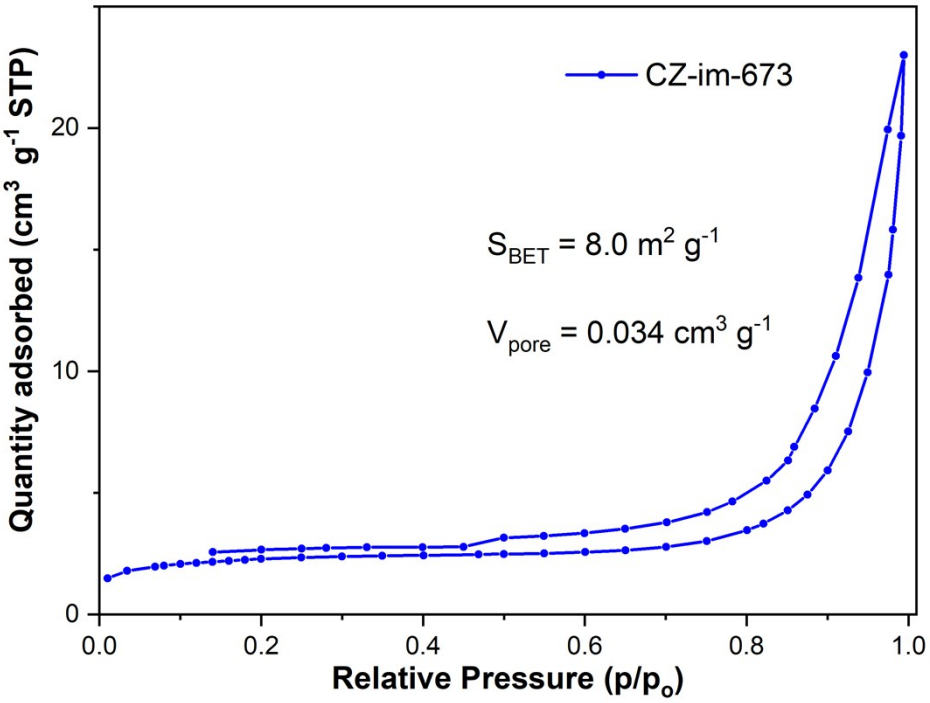

Fig. S9. N_2 physisorption isotherm linear plot of CZ-im-673.

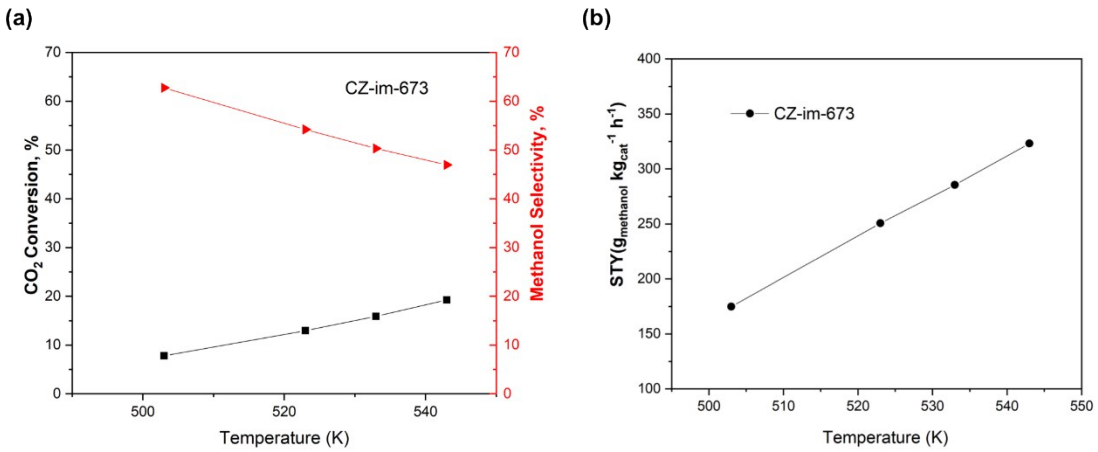

Fig. S10. (a) Methanol selectivity and CO_2 conversion, (b) methanol STY in methanol synthesis from CO_2 hydrogenation over CZ-im-673. Reaction conditions: 4.5 MPa, H_2/CO_2 = 3 and GHSV = 10,800.

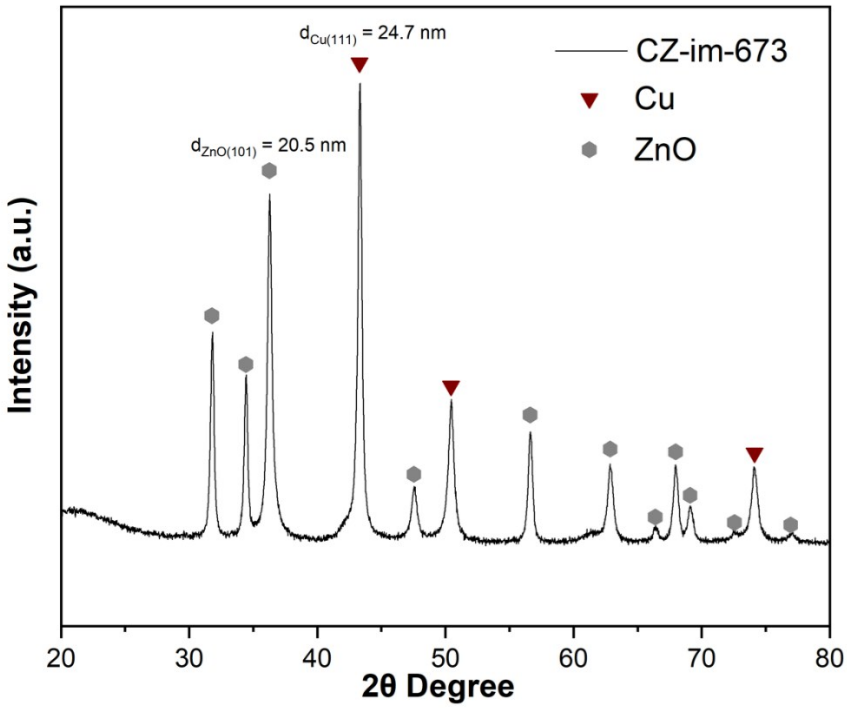

Fig. S11. XRD spectra of CZ-im-673. The crystalline size of Cu and ZnO were calculated by applying the Scherrer Equation.

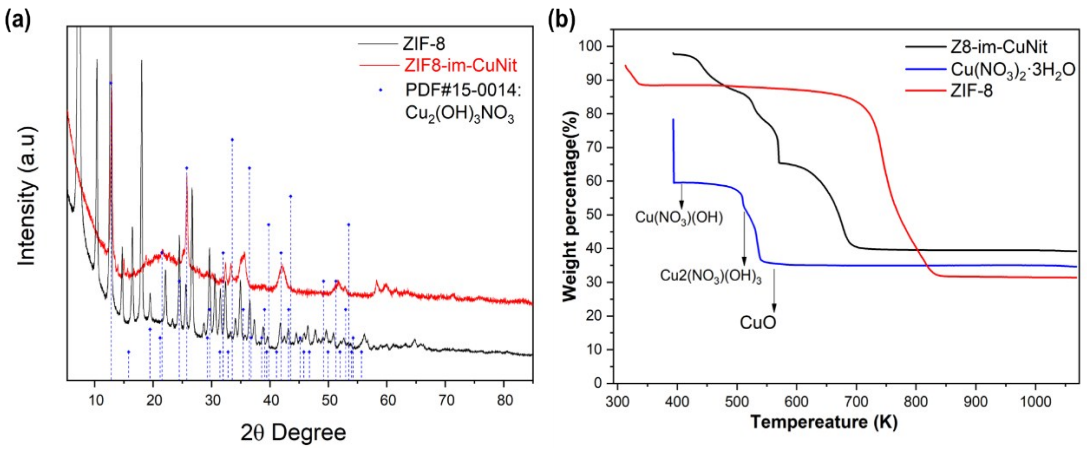

Fig. S12. (a) XRD spectra of ZIF-8, ZIF8-im-CuNit and $Cu_2(OH)_3NO_3$. (b) TG curves of ZIF-8, ZIF8-im-CuNit and $Cu_2(OH)_3NO_3$.

ZIF8-im-CuNit stands for the precursor formed after the impregnation of ZIF-8 with $Cu(NO_3)_2{\cdot}3H_2O$ ethanolic solution and the subsequent solvent evaporation. In (a), the characteristic diffraction peaks of ZIF-8 disappeared on the spectra of ZIF8-im-CuNit while the main peak positions fit well with the standard lines of $Cu_2(OH)_3NO_3$ (PDF#15-0014). In (b), the TG curve of ZIF8-im-CuNit shows similar weight loss behavior to $Cu(NO_3)_2{\cdot}3H_2O$ before 600 K and the decomposition of zinc immidazolate causes the weight loss around 650 K which is 100 K lower than the decomposition temperature of zinc immidazolate framework 8.

Discussion on the concern of formation of standalone ZnO particles

Fig.S13 presents thermal gravimetric data of ZIF-8 and Cu1@ZIF-8. It is obvious that ZIF-8 alone has exceptional thermal stability but after Cu is included the decomposition temperature of ZIF-8 is brought ahead by 150 K, the same phenomenon was found in our previous work about Pd@ZIF-8 (*Appl. Catal. B: Environ.*, **2018**, 234, 143-152). A reasonable explanation could be the ability of oxygen activation by Cu species (instead of innate instability of ZIF-8 due to pore structure change as the blue curve in Fig.S13 demonstrate better stability of reduced Cu1@ZIF-8 under N_2 flow than that under air flow). Thus, we can infer that ZnO grows around Cu surface in a way that Cu surface provides the landing sites for ZnO formation from ZIF-8 decomposition under air atmosphere. These, together with the wide ZnO diffraction peaks or the remarkably small size of ZnO, lead us to believe ZnO particles are mainly generated around Cu particles. This can happen even if Cu particles reside near the surface layers of ZIF-8 as ZIF-8 can collapse and shrink during decomposition, ensuring constant contact with Cu surfaces.

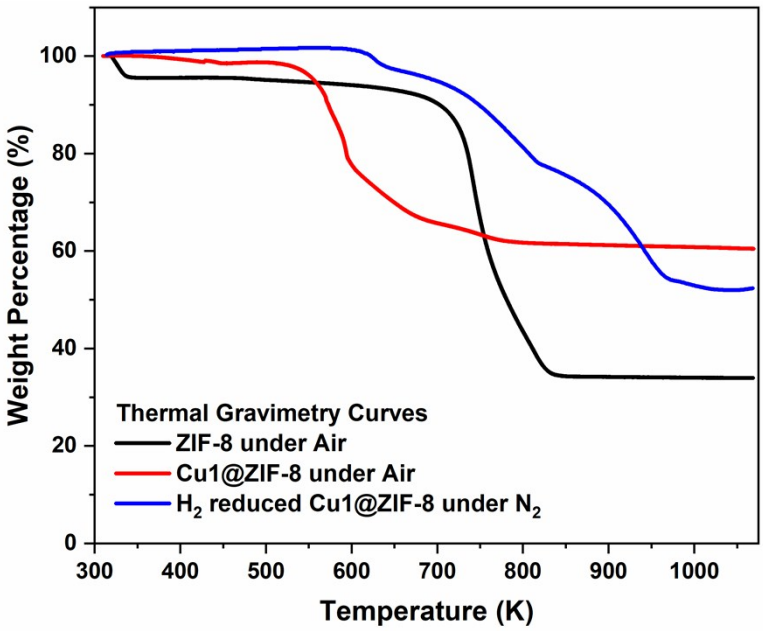

Fig. S13. TG curves of ZIF-8 under air and Cu1@ZIF-8 under air and N_2. The experimental conditions are as follows. The black and red curve are obtained by air atmosphere TG measurement at a heating rate of 10 K min^{-1} on ZIF-8 and as synthesized Cu1@ZIF-8. The blue curve (upper most) is obtained on H_2 reduced (in a tubular furnace with 20 mL min^{-1} 10% H_2/Ar before TG) Cu1@ZIF-8 under N_2 atmosphere at 10 K min^{-1}.

Discussion on the accuracy of crystal size by XRD analysis

We perform the pseudo-Voigt fitting of the XRD peaks and details about crystalline size calculation in Fig. S14. Also, we have put the refinement results in Fig. S15. The phase ratio used is quite reasonable as compared to ICP data. Due to the quality of the diffraction data, it is impossible to get a satisfying result (Rwp<10, GOF<2), though the trend for ZnO size variation complies with those derived from Scherrer equation in Fig. S14. An enlargement of FWHM of the diffraction peaks is clearly seen in Fig. S14, which makes us believe these with Scherrer equation could provide a better analysis of crystalline size.

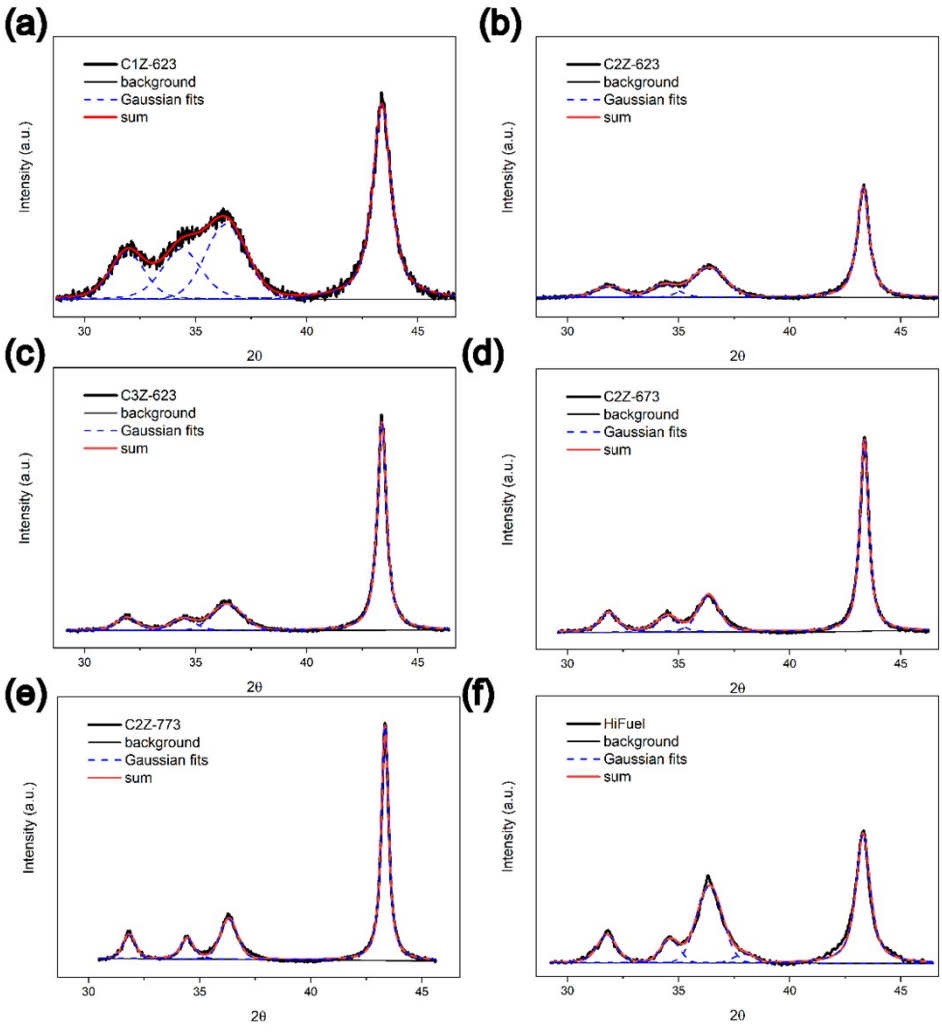

Fig. S14. XRD peak fitting (by pseudo-Voigt function) for the calculation of ZnO size and Cu size. FMHW (full width at half maxima) of the two peaks at 2θ angle of 36.25° (ZnO(101)) and 43.30° (Cu(111)) were substituted into Scherrer equation, d=0.89*0.154 nm/[(FMHW in radians)*cosθ], to derive the particle size.

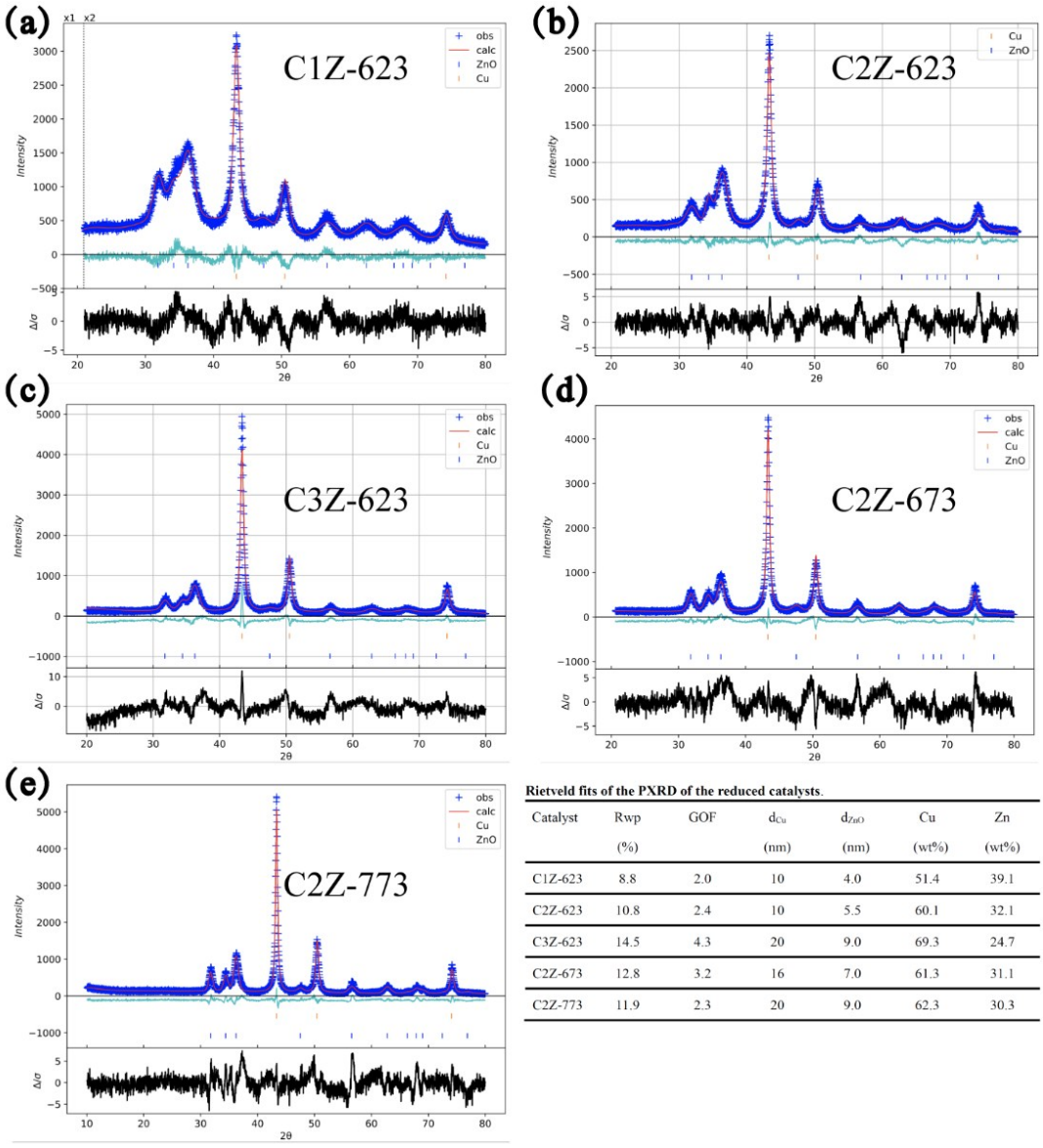

Rietveld fits of the PXRD of the reduced catalysts.

Catalyst	Rwp (%)	GOF	d_{Cu} (nm)	d_{ZnO} (nm)	Cu (wt%)	Zn (wt%)
C1Z-623	8.8	2.0	10	4.0	51.4	39.1
C2Z-623	10.8	2.4	10	5.5	60.1	32.1
C3Z-623	14.5	4.3	20	9.0	69.3	24.7
C2Z-673	12.8	3.2	16	7.0	61.3	31.1
C2Z-773	11.9	2.3	20	9.0	62.3	30.3

Fig. S15. PXRD Rietveld refinement (using GSASII) for (a) C1Z-623, (b) C2Z-623, (c) C3Z-623, (d) C2Z-673, (e) C2Z-773. The goodness of fitting and certain results are shown in the last table.

Discussion on the reaction pathway for RWGS and methanol synthesis

For the forward methanol synthesis reaction over Cu/ZnO catalysts, there has long been suspicion that methanol forms via hydrogenation of surface CO intermediates generated by RWGS reaction. If this is the fact, then slowing down the flow of H_2/CO_2 will benefit the selectivity to methanol as it facilitates further hydrogenation of CO. To check this, we have tested C1Z-623 K under faster flows of H_2/CO_2 at 523 K and 4.5 MPa, the results of which is present in Fig. S16. It can be seen that a higher GHSV leads to a lower CO_2 conversion rate but higher methanol selectivity, which does not support the idea of methanol formation via RWGS-generated CO intermediates. This is in accordance with the result of Schlögl et al. that CO and CH_3OH production on Cu/ZnO undergo different intermediates (Robert Schlögl et al. *Journal of Catalysis* 328 (2015): 43-48.; Pérez-Ramírez et al. *Angewandte Chemie International Edition* 55.37 (2016): 11031-11036.). Besides, the decline in methanol selectivity with increasing temperature is explained by the fact that high temperature is favorable for the endothermic RWGS reaction (41.2 kJ mol^{-1} at 298 K) rather than the methanol synthesis (−49.5 kJ mol^{-1} at 298 K).

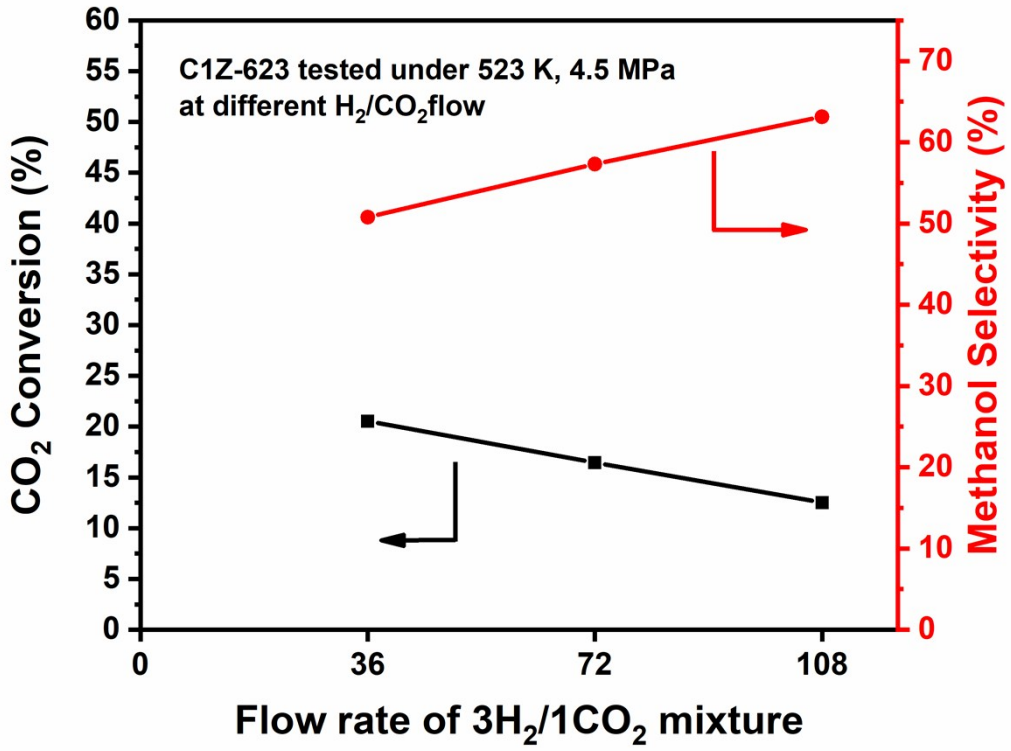

Fig. S16. Catalytic test of C1Z-623 at different flow rate of H_2/CO_2 reactant mixture.

Discussion on the residue N in the catalysts

As for the residue N in the catalysts, we carried out the XPS measurement on C2Z-623 right after calcination, as shown in Fig. S17. In the wide scan, N 1s peak is indiscernible. For the N 1s scan, a very minor signal for N 1s can be recognized. So, we can probably rule out the influence of N doping in this work.

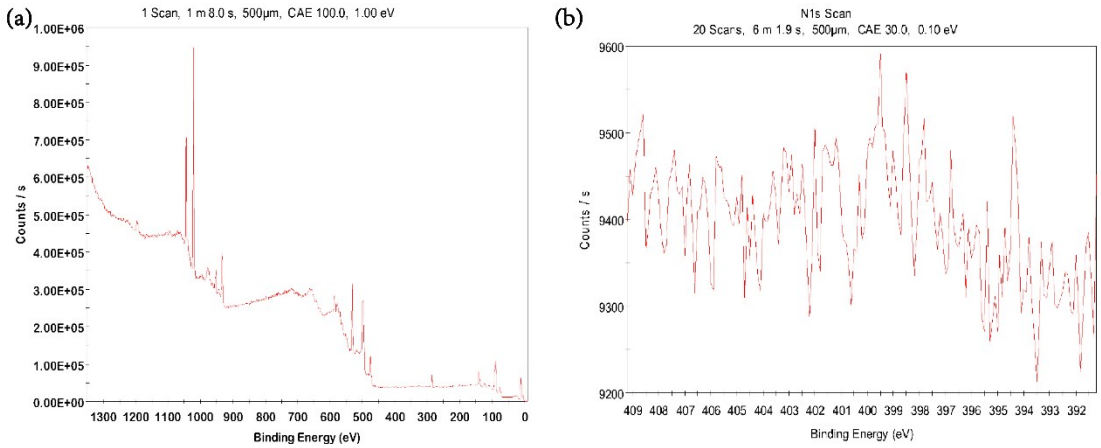

Fig. S17. Wide scan (a) and N1s scan (b) XPS spectra for as-synthesized C2Z-623.

Discussion on the stability of ZIF-8 in the $NaBH_4$ treatment

We have supplemented a contrast experiment as follows: (1) 0.5g ZIF-8 was added into 60 mL of methanol and was magnetically stirred for 1 h at ambient temperature. (2) 20 ml aqueous solution of $NaBH_4$ (0.5260 g, 13.9 mmol) was added into the above dispersion and then maintained under stirring and ambient temperature for 1h. (3) Collect the precipitation by centrifugation and thoroughly wash it by ethanol and water and then vacuum dry it. (4) XRD measurement on thus pre-treated ZIF-8. The XRD patterns of ZIF-8 before and after the treatment are shown in Fig. S18 and it can be seen that the crystallinity remains the same before and after treated by $NaBH_4$.

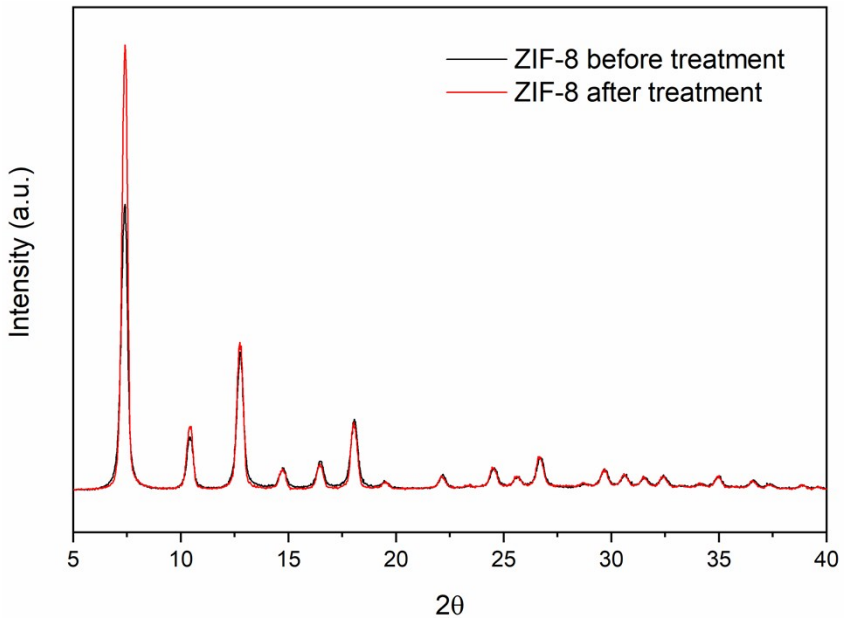

Fig. S18. XRD patterns of ZIF-8 before and after the $NaBH_4$ treatment with the purpose to investigate the stability of ZIF-8 during synthesis of Cu@ZIF-8. The process is as below: (1) 0.5g ZIF-8 was added into 60 mL of methanol and was magnetically stirred for 1 h at ambient temperature. (2) 20 ml aqueous solution of $NaBH_4$ (0.5260 g, 13.9 mmol) was added into the above dispersion and then maintained under stirring and ambient temperature for 1h. (3) Collect the precipitation by centrifugation and thoroughly wash it by ethanol and water and then vacuum dry it.

Table S1 The BET surface area and the porosity of ZIF-8, Cu1@ZIF-8, Cu2@ZIF-8 and Cu3@ZIF-8. The isotherms are demonstrated in Fig. S1.

Samples	S_{BET} (m^2 g^{-1})	$V_{mesopore}$ (cm^3 g^{-1})	$V_{micropore}$ (cm^3 g^{-1})	V_{pore} (cm^3 g^{-1})
ZIF-8	1481.0	0.67	0.64	1.31
Cu1@ZIF-8	1078.9	0.13	0.46	0.59
Cu2@ZIF-8	666.5	0.22	0.26	0.48
Cu3@ZIF-8	656.3	0.35	0.25	0.60

Table S2 Elemental composition data of CxZ-T compared with HiFuel.

Catalyst	Cu content (%)	Zn content (%)
C1Z-623	41.2 (44.2)	38.1 (35.9)
C2Z-623	57.6 (56.9)	21.9 (23.1)
C3Z-623	63.3 (62.9)	16.2 (17.0)
C2Z-673	55.2 (56.9)	23.5 (23.1)
C2Z-773	53.4 (56.9)	24.0 (23.1)
HiFuel	41.8	19.2

Note: Numbers in parenthesis are the nominal values according to the recipe.

Table S3 Quantitative H_2 TPD desorption data.

Catalyst	H_2 α desorption ($\mu mol\ g_{Cu}^{-1}$) [a]	Cu crystalline size by XRD (nm)	ZnO crystalline size by XRD (nm)
C1Z-623	148	7.9	3.7
C2Z-623	92.2	11.9	4.5
C3Z-623	87.0	15.4	4.8
C2Z-673	46.8	16.4	7.1
C2Z-773	39.3	19.6	8.7

[a] H_2 α desorption peak stems from H_2 desorbed before 500 K and the quantity is normalized to per gram of Cu.